



CHORUS

This is the accepted manuscript made available via CHORUS. The article has been published as:

From frustrated to unfrustrated: Coupling two triangular-lattice itinerant quantum magnets

Sahinur Reja, Pavel S. Anisimov, and Maria Daghofer
Phys. Rev. B **96**, 085144 — Published 30 August 2017

DOI: [10.1103/PhysRevB.96.085144](https://doi.org/10.1103/PhysRevB.96.085144)

From Frustrated to Unfrustrated: Coupling two triangular-lattice itinerant Quantum Magnets

Sahinur Reja,^{1,2} Pavel S. Anisimov,³ and Maria Daghofer^{3,4}

¹*Department of Physics, Indiana University, Bloomington, Indiana 47405, USA*

²*IFW Dresden, Helmholtzstr. 20, 01069 Dresden, Germany*

³*Institute for Functional Matter and Quantum Technologies,
University of Stuttgart, Pfaffenwaldring 57 70550 Stuttgart, Germany*

⁴*Center for Integrated Quantum Science and Technology,
University of Stuttgart, Pfaffenwaldring 57 70550 Stuttgart, Germany*

(Dated: July 27, 2017)

Motivated by systems that can be seen as composed of two frustrated sublattices combined into a less frustrated total lattice, we study the double-exchange model with nearest-neighbor (NN) and next-nearest-neighbor (NNN) couplings on the honeycomb lattice. When adding NN hopping and its resulting double exchange to the antiferromagnetic (AFM) Heisenberg coupling, the resulting phase diagram is quite different from that of purely Heisenberg-like magnetic models and strongly depends on electron filling. For half filling, patterns of AFM dimers dominate, where the effective electronic bands remain graphene-like with Dirac cones in all phases, from the FM to the 120° limit. When the density of states at the Fermi level is sizable, we find non-coplanar incommensurate states as well as a small-vortex phase. Finally, a non-coplanar commensurate pattern realizes a Chern insulator at quarter filling. In the case of both NN and NNN hopping, the noncoplanar spin pattern inducing Chern insulators in triangular lattices is found to be quite stable under coupling into a honeycomb system. The resulting total phases are topologically nontrivial and either a Chern insulator with $C = 2$ or a magnetic topological crystalline insulator protected by a combination of mirror-reflection and time-reversal symmetries arise.

PACS numbers: 71.27.+a, 75.10.Hk, 75.10.Lp, 75.40.Mg

I. INTRODUCTION

Frustration in magnetic systems is currently a topic of high interest, because it can support a variety of unconventional states by suppressing more standard ordered states that may arise without it. Examples are spin liquids^{1,2} and spin ice,^{3,4} where magnetic moments do not fully order even at the lowest temperatures, or non-coplanar magnetic patterns. The latter may arise through an interplay of spin-orbit coupling and magnetism, e.g. in the case of skyrmions⁵ and vortex crystals,^{6,7} or via the competition⁸⁻¹⁰ of antiferromagnetic (AFM) superexchange and kinetic energy of electrons, which tends to prefer ferromagnetic (FM) order.

Frustration can have various sources, from lattice geometry over orbital symmetries to more generally competing tendencies in a Hamiltonian. Accordingly, it can also be lifted in a variety of ways. Here we focus on frustration due to lattice geometry in combination with competition between kinetic and super-exchange energy. Frustration might then on one hand be lifted by changing the balance between kinetic and magnetic terms (e.g. by doping), but on the other hand also by changing the lattice from frustrated to unfrustrated. This second mechanism is currently under debate in double-perovskite systems, which are composed of two interpenetrating face-centered-cubic lattices, made up from ions of one element each.¹¹⁻¹⁴ Each separate lattice is then highly frustrated, but the combined one is simple cubic and unfrustrated. How strong the sublattices are connected – and thus the

degree of frustration – depends on the specific compound.

Here, we address such a mechanism in a much simpler setting, namely by coupling two triangular lattices (frustrated) into a honeycomb one (unfrustrated). This geometry is potentially also applicable to materials, namely to bilayers,¹⁵ where each layer forms a triangular lattice and where the top layer is shifted with respect to the bottom layer, so that each ‘top’ site lies in the middle of a triangle formed by ‘bottom’ sites. With this in mind, the half-filled Hubbard model has recently been studied for the same geometry, i.e., a honeycomb model with (unfrustrated) first- and (frustrated) second-neighbor hopping.¹⁶ The phase diagram was shown to contain stripes, spirals and phases with non-coplanar magnetism with trivial and non-trivial Chern numbers $C = 0, 2$, which were ascribed mainly to magnetic frustration of the super-exchange mechanism. Interestingly, the spin pattern giving $C = 2$ in the frustrated half-filled honeycomb lattice has also been reported to be stabilized by a van-Hove singularity in the unfrustrated quarter-filled model without second-neighbor hopping.^{17,18}

We focus here on the Kondo-lattice model describing itinerant electrons coupled to localized magnetic moments. On one hand, this is motivated by the potentially more complex physics of double perovskites with localized and itinerant carriers,¹⁹ on the other, magnetic interactions and electron itineracy can here be addressed separately. The Kondo-lattice model has been studied in detail on both the triangular and the honeycomb lattice. On the triangular lattice, one of the most intriguing

ing phases is a quantum anomalous Hall (QAH) state, where a non-coplanar spin pattern induces non-trivial band topology.^{20,21} At the same density, the honeycomb system shows in addition to straightforward FM and Néel AFM states also effects such as massive, but sub-extensive, ground-state degeneracy and emergent frustration due to a spontaneous triangular superstructure.²² Perhaps not surprisingly, we will find here that coupling two triangular lattices yields phases reminiscent of either case.

Without kinetic energy, i.e. for localized Heisenberg spins, the interpolation between triangular and honeycomb lattices has been addressed extensively. The resulting J_1 - J_2 -($-J_3$) honeycomb model has revealed a rich phase diagram with several incommensurate, but coplanar, spiral phases.^{23,24} We are going to see here how the kinetic energy of charge carriers modifies this picture and that it can not be captured by an effective FM coupling. One important difference is that the kinetic energy will be seen to favor commensurate patterns or non-coplanar states over incommensurate spirals. Finally, issues related to ours have also been discussed²⁵ for a frustrated honeycomb Kondo-Heisenberg model. In this study, localized spins were in the quantum limit $S = 1/2$ and antiferromagnetically coupled to electrons; an important result is the replacement of Néel antiferromagnetism by disordered valence-bond states. In our case of large spins, whose moment cannot be balanced by the conduction electrons, order is not destroyed, even though we similarly find phases, where electron motion is confined to small units like dimers or hexagons.

We are going to analyze two scenarios, a ‘purely magnetic’ frustration, where hopping is restricted to nearest neighbors and where nearest-neighbor (NN) and next-nearest-neighbor (NNN) spin exchange interpolates between the limits of Néel-AFM order and the 120° pattern of the Yafet-Kittel state. Among the variety of phases supported by this interplay, we find effects like vortex patterns and non-coplanar spiral-like phases, but also a QAH phase with Chern number $C = 1$.

The second scenario involves strong second-neighbor hopping, where each triangular lattice is in a topologically non-trivial QAH state. When coupling them together into a honeycomb system, we can find a Chern insulator with $C = 2$, as the phase reported for the Hubbard model.^{16–18} There is additionally a phase with opposite chiralities in the sublattices, which has Chern number $C = 0$, but is nevertheless topologically nontrivial: a combination of time reversal and mirror reflection protects edge states on zig-zag edges, leading to a state similar to a topological crystalline insulators (TCI),²⁶ but with underlying magnetic order.

After introducing the model and the method in Sec. II, we present results with unfrustrated NN hopping and purely magnetic frustration in Sec. III A. We discuss two electron densities, half filling $n = 1/2$ (Sec. III A 1) and $n = 2/3$ (Sec. III A 2) with very different density of states at the Fermi level in order to draw out the impact of the

kinetic energy. We then include second-neighbor hopping in Sec. III B, where we focus on $n = 1/2$, because this filling shows the QAH state on the triangular lattice. We discuss in particular the emergent TCI and its symmetries Sec. III B 3. Section IV offers a summary and conclusion.

II. MODEL AND METHOD

We consider a honeycomb double-exchange model with NN and NNN terms. For dominant NNN parameters, this corresponds to two triangular lattices that are connected via the NN terms. The model describes itinerant fermions that interact with localized spins via Hund’s rule coupling. For localized spins large enough to be treated classically and dominant Hund’s rule coupling, one can focus the discussion to itinerant fermions whose spin is parallel to the localized spins.²⁷ If we assume that the localized spins moreover interact with each other, the model Hamiltonian becomes

$$\begin{aligned}
 H = & -t_1 \sum_{\langle ij \rangle} (\Omega(\mathbf{S}_i, \mathbf{S}_j) c_i^\dagger c_j + H.c.) \\
 & - t_2 \sum_{\langle\langle ij \rangle\rangle} (\Omega(\mathbf{S}_i, \mathbf{S}_j) c_i^\dagger c_j + H.c.) \\
 & + J_1 \sum_{\langle ij \rangle} \mathbf{S}_i \cdot \mathbf{S}_j + J_2 \sum_{\langle\langle ij \rangle\rangle} \mathbf{S}_i \cdot \mathbf{S}_j \quad (1)
 \end{aligned}$$

where c_i (c_i^\dagger) is the annihilation (creation) operator for an electron with spin parallel to the local magnetic moment \mathbf{S}_i . Angular brackets $\langle ij \rangle$ and $\langle\langle ij \rangle\rangle$ denote NN and NNN pairs of sites on a honeycomb lattice. J_1 and J_2 give the strengths of Heisenberg intersite coupling. t_1 and t_2 parameterize NN and NNN hopping, which is however decisively modified by the local spin structure: As the spin of electron always has to point along the local quantization axis $\parallel \mathbf{S}_i$, the relative spin orientation enters via $\Omega(\mathbf{S}_i, \mathbf{S}_j) = [\cos(\theta_i/2) \cos(\theta_j/2) + \sin(\theta_i/2) \sin(\theta_j/2) e^{-i(\phi_i - \phi_j)}]$, with polar and azimuthal angles $\{\theta_i, \phi_i, \theta_j, \phi_j\}$.^{28,29}

The model is investigated using a Markov-chain Monte Carlo (MCMC) method which combines the classical Monte Carlo for spins with the diagonalization of the fermion degrees of freedom.²⁹ The solution of a fermionic problem is required at each Monte Carlo update step in order to obtain the electronic contribution to the total energy of a given classical configurations of localized spins. As this fermion problem is a non-interacting one, however, it remains tractable for larger clusters and as the spins are classical, no sign problem arises in the Monte Carlo. The fermions only interact via their impact on the localized spins. As we are here interested in the ground-state phase diagram rather than in temperature-driven phenomena, we complement the MCMC with a subsequent numerical optimization starting from the last MCMC configuration.

We additionally implemented an alternative algorithm based on a Chebychev expansion of local Green's functions rather than full diagonalization.³⁰ For each local MCMC update, only four Green's functions need to be evaluated, which can be achieved by a recursive Chebychev scheme based on two initial vectors. The scheme has a much better scaling with the number of sites N , only $\propto N$ rather than $\propto N^3$ as for full diagonalization.³¹ However, the Chebychev-based algorithm did not extend attainable system sizes significantly, because our most difficult cases, the incommensurate noncoplanar states discussed in Sec. III A 2, require very low temperatures. In this regime, the number of Chebychev polynomials needed becomes so large that runtimes would only be improved for cluster sizes beyond the reach of full MCMC simulations.

We calculate the ground state energy using this Monte-Carlo method at different values of the Hamiltonian's parameters. We then identify the respective magnetic order and, where appropriate, compare the energy obtained in Monte Carlo with that of the perfectly ordered state. In addition to looking at and comparing real-space spin configurations, we make use of the spin structure factor

$$S(\mathbf{q}) = \frac{1}{N^2} \sum_{ij} \mathbf{S}_i \cdot \mathbf{S}_j e^{-i\mathbf{q} \cdot (\mathbf{r}_i - \mathbf{r}_j)}. \quad (2)$$

where N is the number of sites and $\mathbf{r}_i, \mathbf{r}_j$ are the positions of sites i, j . As the honeycomb lattice has a two-site unit cell, momentum \mathbf{q} from the first two Brillouin zones can be relevant. The observable was evaluated from the optimized ground-state configuration.

III. RESULTS AND DISCUSSION

A. Connecting two frustrated antiferromagnets

As a first example, we discuss NN hopping $t_1 = 1$ and NNN magnetic interaction $J_2 > 0$, i.e., $t_2 = 0$ and $J_1 = 0$. This case thus describes two triangular Heisenberg antiferromagnets that are coupled by electron itineracy. The kinetic energy tends to favor FM spin alignment, because this maximizes band width; the two limiting cases are thus (i) two decoupled triangular lattices with 120° pattern (for $J_2 > 0$ and $t_1 = 0$) and (ii) one FM honeycomb lattice (for $J_2 = 0$ and $t_1 \neq 0$). Intuitively, the intermediate case might then seem similar to the J_1 - J_2 model discussed in Refs. 23 and 24, where coplanar incommensurate spirals interpolate between these limits.

However, the rule of thumb that electron itineracy favors FM alignment is often modified by more complex effects due to the phases of the effective hoppings.²⁸ In particular, magnetic patterns are favored if they open a band gap at the Fermi level. The impact of the kinetic energy accordingly depends on the band structure as well as on filling. We are here going to discuss two fillings, $n = 1/2$ (i.e. one electron per two sites) and $n = 1/3$ or

$2/3$ (1 or 2 electrons per 3 sites). As the kinetic energy is in this section restricted to the NN bonds, i.e. lives on the bipartite honeycomb lattice, it is particle-hole symmetric and $n = 1/3$ is equivalent to $n = 2/3$ in the limit of infinite Hund's rule studied here.

For spinless fermions not coupled to any localized spins, or alternatively for an FM system, the two chosen filling fractions correspond to very different Fermi surfaces: At $n = 1/2$, the density of states vanishes in a pseudogap at the Fermi level, while $n = 1/3$, resp. $n = 2/3$ corresponds to a substantial density of states. Mechanisms related to the kinetic energy can thus be expected to play out quite differently in these two scenarios. One feature where coupling via the kinetic energy has previously been found to differ qualitatively from FM exchange is that all states seen in the J_1 - J_2 (- J_3) model are coplanar, while Kondo-lattice models are known to support non-coplanar states like the (gapped) QAH state of the half-filled triangular lattice.²⁰ Indeed, we are here going to see that the phase diagram for $n = 1/2$, with a weaker impact of the band structure, consists predominantly of coplanar patterns while the $n = 1/3/n = 2/3$ filling supports non-coplanar states over wide parameter ranges.

1. Dominant AFM dimers and coplanar order at $n = 1/2$

Without J_2 , the system is of course FM. MCMC simulations for 12×12 sites at small J_2 show a spiral that is FM along an armchair edge (i.e. the vertical direction in Fig. 2) and has the largest period allowed by the lattice along zig-zag (i.e. the horizontal direction in Fig. 2). This effect is well known for Kondo-lattice models,^{22,32-34} as the spiral winning over FM order always has the largest possible period and thus converges to the FM state in the thermodynamic limit, it should be considered a finite-size effect. It shows, however, that our simulations reliably resolved the small energy difference to the FM pattern.

For vanishing $t_1 = 0$, we expect each sublattice to show the 120° pattern of the YK state, and this is indeed also found for finite t_1 , namely at $J_2 \gtrsim 0.3t_1$. J_2 can by itself of course not decide the relative orientation of the two sublattices. Moreover, J_1 cannot fix the relative orientation either, because the three nearest neighbors of each spin are always oriented along the three directions of the 120° pattern, so that the total NN interactions always cancel. In the J_1 - J_2 Heisenberg model, incommensurate order, which distorts the 120° arrangement, arises instead. Here, however, finite t_1 stabilizes a pattern with perfect 120° order within the sublattices and where each spin has one FM nearest neighbor; the NN FM dimers lie along one of the lattice's zig-zag directions, see Fig. 2(d).

Such FM dimers turn out to dominate most of the phase diagram. The original three-fold rotation symmetry is broken by the dimers: they are put onto the lattice so that exactly one of the zig-zag directions does *not* con-

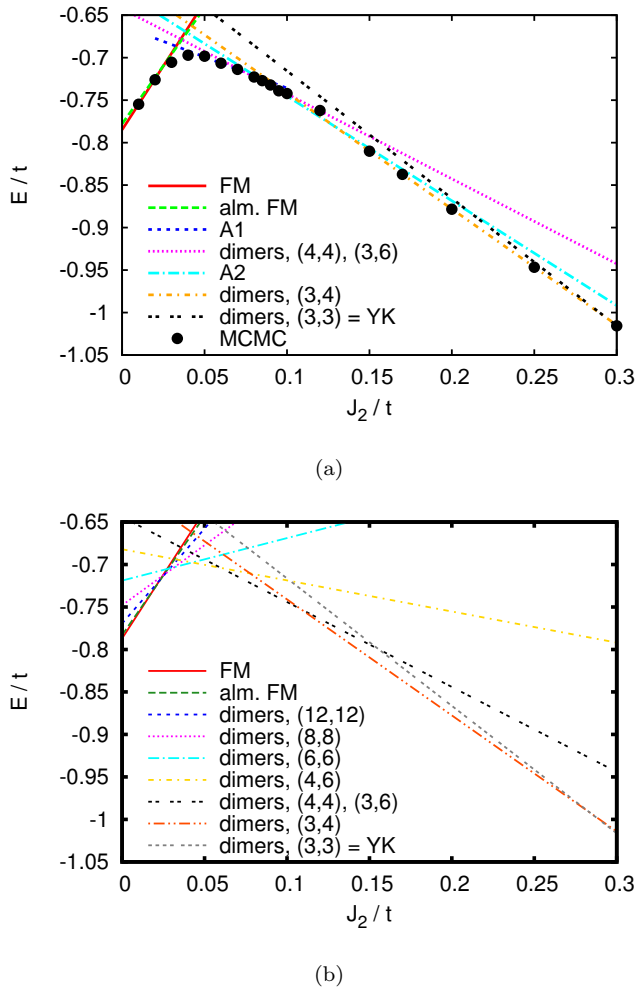


FIG. 1. (Color online) Different phases with increasing J_2 at $n = 1/2$. (a) Comparison MCMC energies (full circles) with the energies (straight lines) calculated for perfect spin configurations, lattice size 12×12 . (b) Ground-state energies of candidate phases inferred from (a), but for 24×24 sites. Apart from the FM regime at very small J_2 , most of the phase diagram is dominated by ‘dimer’ phases, where FM dimers are arranged along one zig-zag direction. The phases can then be characterized by their periodicity along the other two – still equivalent – zig-zag directions. For the smallest unit cell with a periodicity of 3 along both axes, spins within each triangular sublattice form the 120° pattern of the Yafet-Kittel (YK) state. $J_1 = 0$ and $t_2 = 0$

tain dimers. The relative orientation of the dimers can then have different periodicity along the two remaining equivalent zig-zag directions. The 120° YK pattern found at large J_2 corresponds to periods of three along both directions. Intermediate values of J_2 stabilize larger-unit-cell patterns, on the 12×12 lattice, we find, e.g., $(6, 3)$ and $(4, 4)$ (with the same energies) and $(4, 3)$ at rather large J_2 , see Fig. 2.

The dimer phases compete with spiral phases that can be seen as modifications of an ‘A-phase’ pattern where

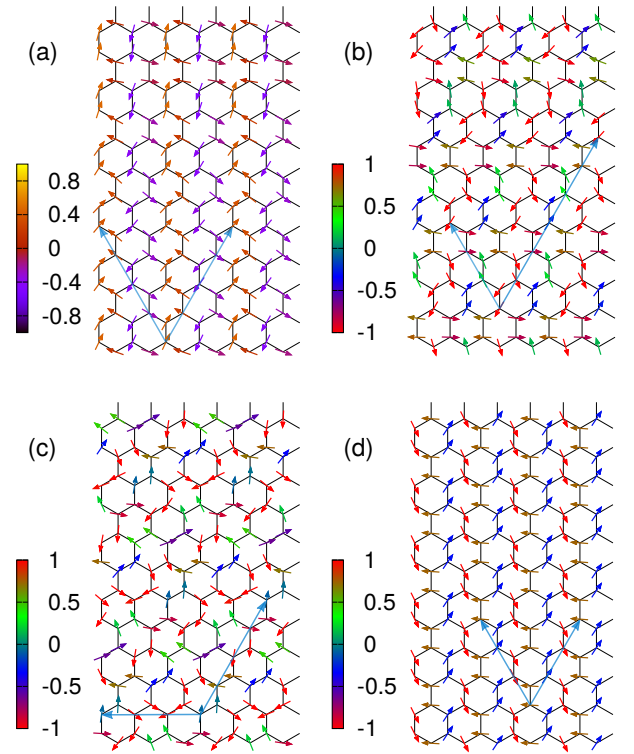


FIG. 2. (Color online) Dimer phases with different periodicities as obtained by MCMC and optimization for 12×12 sites, periodicities are indicated by large (light blue) arrows. (a) Periodicities $(4, 4)$ for $J_2 = 0.08t_1$, (b) periodicities $(3, 6)$ for $J_2 = 0.1t_1$, (c) periodicities $(3, 4)$ for $J_2 = 0.2t_1$, (d) periodicities $(3, 3)$ for $J_2 = 0.3t_1$. The last pattern has the 120° YK pattern within each sublattice. Color indicates the out-of-plane component of the spins. Armchair and zig-zag directions run along the vertical and horizontal directions, resp.

each spin has two FM and one AFM neighbor. In this underlying pattern, the FM bonds then run along a zig-zag direction, orientation between zig-zag chains is AFM. The patterns actually seen in the simulations are modifications where either the FM zig-zag (‘A2’) or the AFM armchair (‘A1’) direction has an additional modulation with periodicity 12, i.e., the largest one compatible with the lattice. In the latter A1 case, the FM direction is moreover not perfectly FM, but involves some canting; this canting angle was numerically optimized for the energy comparison to the MCMC data shown in Fig. 1(a). Finally, MCMC results at the transition from the ‘almost FM’ to the ‘A1’ phase ($J_2 \approx 0.04$) are unclear: there might be a small parameter window with non-coplanar order.

While MCMC simulations are not feasible for much larger lattices, comparison of ground-state energies was extended to a 24×24 -site lattice, see Fig. 1(b). We compared all phases seen on the smaller lattice, with the large periodicity of the ‘almost FM’ and ‘almost A phase’ spirals adjusted to the larger lattice, as well as all dimer

patterns compatible with 24×24 sites. Of these, the Figure only includes phases that are the ground state for some range of J_2 . We see that the modulated A phases are now replaced by dimer arrangements, whose unit cell shrinks with increasing J_2 .

At half filling, the competition between NNN J_2 and NN t_1 thus largely plays out via the formation of FM dimers, which are themselves arranged in periodic patterns. For rather small $J_2 \lesssim 0.1$ close the FM phase, the periodicity becomes large, so that the thermodynamic limit can show incommensurate order. For intermediate and large J_2 , patterns are commensurate, in contrast to the J_1 - J_2 Heisenberg model. Similar to Heisenberg models, on the other hand, is the fact that observed phases are coplanar.

Interestingly, the one-particle spectral density for all dimer patterns remains – as for the FM phase – graphene-like with Dirac cones. Hoppings are anisotropic, as they are reduced for two of the three honeycomb bond directions: hoppings remain t_1 for the bonds supporting dimers, they are $t_1 \cos(\pi/n_{a/b})$, with $n_{a/b}$ referring to the two periodicities, along the other two kinds of bonds. Accordingly, band width is somewhat reduced and the location of the Dirac cones changes, but features like the linear dispersion and the pseudogap remain. While the electronic energy contribution is modified by the renormalized band width, dimer states are not stabilized by the opening of a band gap – at most, they can profit from the fact that the Dirac-cone pseudogap is not filled.

The pure honeycomb double-exchange model at half filling, i.e. for $J_2 = 0$, has been studied in Ref. 22 and the dimer motif discussed here connects to this previous case. For relatively strong $J_1 \geq 0.2t_1$, the J_1 - t_1 models is dominated by FM or slightly canted dimers that lie on bonds along one zig-zag direction and AFM coupled. The salient feature is that after fixing directions on one zig-zag line, two degenerate possibilities exist for assigning spins on each subsequent line. As a result, the system has a large, but subextensive, degeneracy. In contrast to similar phases in compass models,³⁵ but similar to an even more complex model involving additionally lattice degrees of freedom,³⁶ this is not connected to any underlying symmetry of the Hamiltonian. We verified that this physics remains stable in the presence of J_2 , e.g. for $J_1 = 0.5t_1$ and $J_2 = 0.2t_1$. This corroborates the previous finding that such highly degenerate phases building on emergent symmetries arise readily in double-exchange models.

2. Incommensurate and non-coplanar states at $n = 2/3$

Let us now discuss a filling of $n = 2/3$, where the Fermi level for the FM system falls into a region with quite a high density of states. Accordingly, the kinetic energy can be expected to have a larger impact. We indeed consistently find one signature feature that distinguishes frustrated itinerant-electron physics from Heisen-

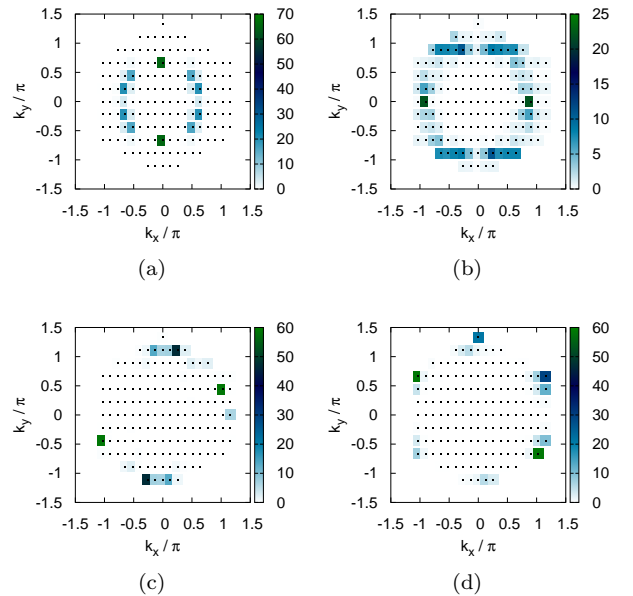


FIG. 3. Spin-structure factor in the first Brillouin zone for a filling of $n = 2/3$ (or $n = 1/3$) and (a) $J_2 = 0.02t_1$, (b) $J_2 = 0.04t_1$, (c) $J_2 = 0.12t_1$ and (d) $J_2 = 0.16t_1$. Obtained by MCMC and subsequent optimization for 18×18 sites; $J_1 = 0$ and $t_2 = 0$.

berg spin models: for intermediate J_2 , the phase diagram is dominated by non-coplanar states.

Due to the frustration, these non-coplanar states are incommensurate – unfortunately, this makes finite-size effects much more severe. The diagonalization of the independent-electron problem does not scale well with system size; we nevertheless simulated the system for up to 18×18 sites. Many features remain qualitatively similar for the whole range $0.02 \lesssim J_2 \lesssim 0.16$: Spins are non-coplanar and several momenta, whose distance from the zone center grows with J_2 , contribute to the spin-structure factor, see Fig. 3. Furthermore, the one-particle spectral density (not shown) is at least suppressed, if not clearly gapped, at the Fermi level.

In some of the observed patterns, spins point with a similar probability in any directions, while they are not distributed so isotropically in others. Similarly, rotational symmetry is found to be broken for many values of J_2 , as can be seen in the spin-structure factor shown in Fig. 3, but not always. Given the current limitations on system size, we cannot establish whether this is a true phase competition or a finite-size effect. There are no indications for appreciable charge-density modulations, nor can we observe skyrmion-like patterns, as have recently been reported for the triangular-lattice model.³⁷ Even though skyrmions would go together with noncoplanar and incommensurate patterns, their identification and clear separation from competing phases might also need larger lattices. We implemented an alternative algorithm based on local Green's functions rather than full diag-

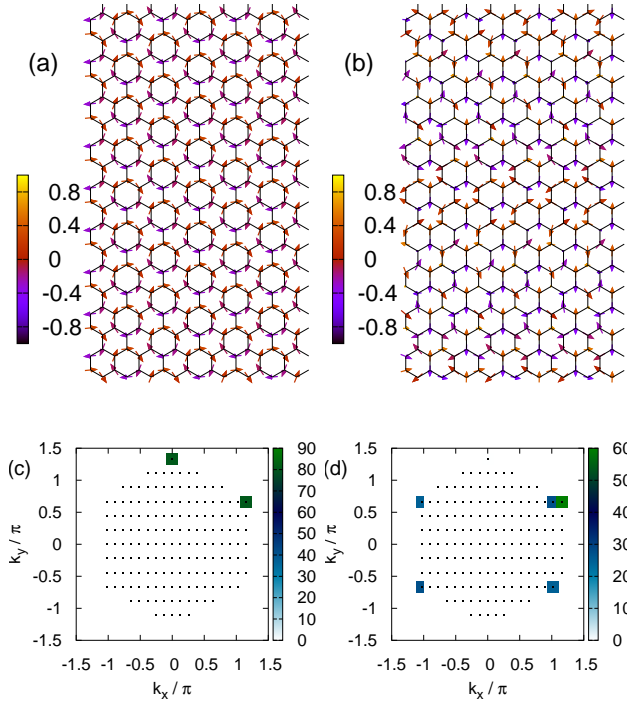


FIG. 4. (Color online) Disconnected vortices for large J_2 and a filling of $n = 2/3$ (equivalent to $n = 1/3$). The disconnected vortices can be seen in (a), which was obtained by MCMC and additional numerical optimization for 18×18 sites and $J = 0.3t_1$. (b) shows the slightly distorted (noncoplanar) pattern found for $J_2 = 0.25t_1$. (c) and (d) are the corresponding spin-structure factors for $J = 2 = 0.3t_1$ and $J_2 = 0.25t_1$, resp. $t_2 = 0$ and $J_1 = 0$.

onalization,³⁰ but this did not extend available cluster sizes sufficiently.

For large $J_2 \gtrsim 0.3t_1$, MCMC simulations for 18×18 sites show that spins within each triangular layer form a 120° YK state in order to satisfy J_2 , so that the spin-structure factor is peaked at the K points, i.e. the corners of the Brillouin zone, see Fig. 4(c). At $n = 2/3$, the electronic kinetic energy aligns the two 120° patterns so that a ‘vortex crystal’ arises, where the vortices form a triangular lattice. Going around a vortex, spins rotate by 60° between sites, see Fig. 4(a). Each vortex is connected to 6 neighboring vortices by NN bonds, but these bonds always contain spins with perfectly AFM orientation. Electrons can thus not hop from vortex to vortex, hence the name ‘disconnected-vortex’ phase.

The purely magnetic energy, i.e., the contribution from J_2 (and actually even from any J_1) is the same as for the 120° dimer pattern seen at $n = 1/2$. The kinetic energy, however, is very different from the graphene-like bands of the dimer state. As vortices are connected by AFM bonds, electrons are filled into levels available on each six-site ring. States located on different vortices are perfectly degenerate. At first sight, six sites with periodic boundary conditions would lead us to expect four states, corresponding to $k = 0, \frac{\pi}{3}, \frac{2\pi}{3},$ and π , of which

the middle two would be twofold degenerate. However, the spin canting within the ring not only reduces the hopping strength, but also adds an additional phase factor so that the allowed momenta become $k = \frac{\pi}{6}, \frac{\pi}{2},$ and $\frac{5\pi}{6}$, all doubly degenerate. This phase is thus expected to be favorable at fillings like $n = 1/3$ and $n = 2/3$, but not at $n = 1/2$, where the Fermi level would be found at a particularly *high* density of states.

For slightly smaller values of $J_2 \approx 0.25t_1$, i.e., just before the onset of the commensurate disconnected-vortex phase, we find a very similar pattern that carries an additional incommensurate and non-coplanar modulation on long length scales, see the configuration in Fig. 4(b). The spin-structure factor accordingly has components slightly off the K point in addition to a signal at K , see Fig. 4(d). The three sharp peaks of the density of states split, but the splitting is almost symmetric and the Fermi level remains within a gap, so that the change in kinetic energy is small. Comparing 12×12 and 18×18 sites and noting that the additional spin-structure peaks are as close to K as possible, we conclude that larger lattices would only show the disconnected-vortex state at even higher values of J_2 . However, similar to the ‘almost FM’ state discussed above, the pattern becomes ever more similar to the disconnected-vortex state and the splitting in the density of states ever smaller.

B. Topologically non-trivial states related to non-coplanar Chern Insulators

We next address the states with topologically nontrivial bands, which we find if either NN Heisenberg exchange J_1 or NNN hopping t_2 are added into the mix. These states can be identified by their non-coplanar spin patterns and their edge states, see figures below, and by explicitly calculating Chern numbers, where we used standard methods.³⁸

1. Chern Insulator at Quarter filling

At quarter filling, we observe the commensurate non-coplanar pattern shown in Fig. 5 if two triangular Heisenberg models are coupled into a honeycomb system by t_1 as well as J_1 . We find this phase to be stable for $t_1 \lesssim J_1 \lesssim 3t_1$ and $J_2 \approx 0.5J_1$, i.e., for roughly comparable interactions. It unit cell contains eight sites, four on each sublattice. The four spins of the unit cell within one sublattice point to the four corners of a tetrahedron and the same four directions arise on both sublattices, see Fig. 5(b) as third neighbors are always parallel. It has an inherent chirality on each sublattice, and the two are parallel.

For the honeycomb *Hubbard* model, the same pattern was discussed at electron filling $n = 3/8$, where it is helped by the van-Hove singularity,^{17,18,39} and is expected to compete with a collinear pattern at finite temperature.³⁹

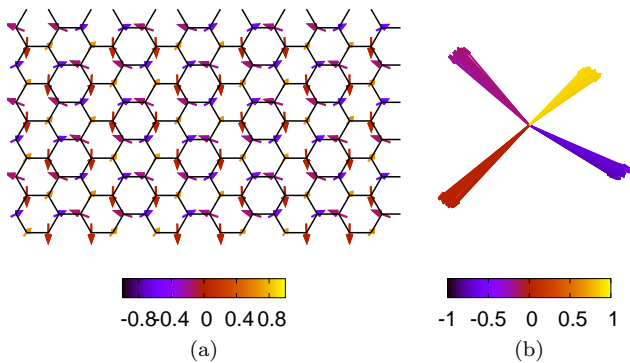


FIG. 5. Chiral non-coplanar pattern at quarter filling for $t_1 = -1$, $J_1 = 1.25|t_1|$, and $J_2 = 0.5|t_1|$. (a) shows the spin pattern. In (b), all spins are drawn to start from the origin and neatly fall along four non-coplanar directions. As can be seen in (a), all four of these directions arise on each sublattice, so that we find the pattern of Refs. 17, 18, and 39.

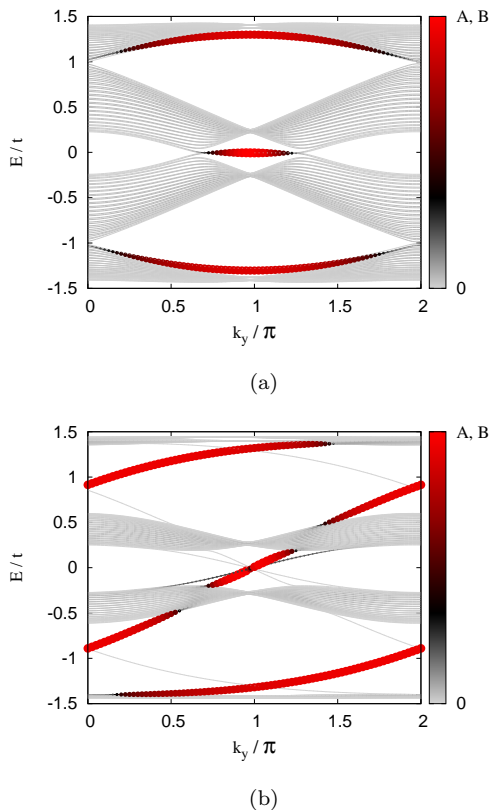


FIG. 6. Edge states for the chiral pattern at quarter filling. Shown are eigenenergies of the phase shown in Fig. 5 when put onto a cylinder. Width and shading of the line indicate weight of the corresponding eigenstate on the top edge. In (a) $t_2 = 0$ and there are Dirac nodes, while $t_2 = -0.2|t_1|$ opens gaps in (b).

In the Kondo-lattice model, the phase is not stabilized by a full gap, but by a suppression of the density of states near the Fermi level: four subbands arise that are connected to their neighbors by Dirac points. Correspondingly, fillings the density of states is lowered for $n = 1/4$ and $n = 3/4$. (At $n = 1/2$, nonmagnetic density of states already has Dirac-cones and a pseudogap.) The van-Hove filling $n = 3/8$ would, in contrast, lie in the middle of a subband, so that it does here not easily support such a state.

Allowing finite $t_2 \neq 0$ opens full gaps, see Fig. 6, while still yielding the same spin pattern (not shown) in MCMC simulations. The gaps are topologically nontrivial such that the system has now four bands, the lower two with $C = 1$ and the higher two with $C = -1$. (Or the other way around for inverted chirality.) For a system put onto a cylinder, edge states accordingly cross the bands gaps, two of them running in parallel for the middle gap that would correspond to half filling. One edge runs across the Fermi level at quarter filling, and the system is a Chern insulator with $|C| = 1$. Coincidentally, $t_2 = -0.2t_1$ also makes the lowest band very flat, see Fig. 6(b), yielding a promising stage to study interacting and topologically nontrivial systems.⁴⁰

2. Topologically nontrivial states from coupled triangular-lattice Chern insulators

At half filling, the triangular Kondo-lattice model with purely NN hopping $|t_1| = 1$ supports a robust QAH phase,²⁰ for both AFM NN exchange $J_1 > 0$ ²¹ and for finite Hund's rule coupling.⁴¹ Its spin pattern corresponds to one sublattice of the pattern discussed above, i.e., to one sublattice of Fig. 5(a). The band gap at the Fermi level that stabilizes the pattern separates two Chern bands with $C = \pm 1$.

We now consider the case of coupling two such half-filled triangular-lattice Chern insulators into a honeycomb system. Let us for simplicity first discuss a purely magnetic coupling, i.e. without hopping between the sublattices. If the magnetic inter-lattice coupling is weak enough to preserve the chiral non-coplanar pattern within each sublattice, we expect to find just two copies of the Chern bands. The Chern numbers can either be the same in both sublattices or opposite to each other. In the first case, the two edge states run in parallel, in the second, they run opposite to each other: if the state from sublattice A runs to the right on the top edge, then the state from sublattice B runs to the left.

When the coupling between sublattices is via hopping, two questions arise, (i) what effective magnetic coupling and consequently total spin pattern arises and (ii) what is the topological character of the combined band. Concerning the effective coupling, it turns out to be weak, presumably due to the fact that each triangular lattice is already gapped at the Fermi level. As the AFM and FM configurations turn out to be extremely close in energy,

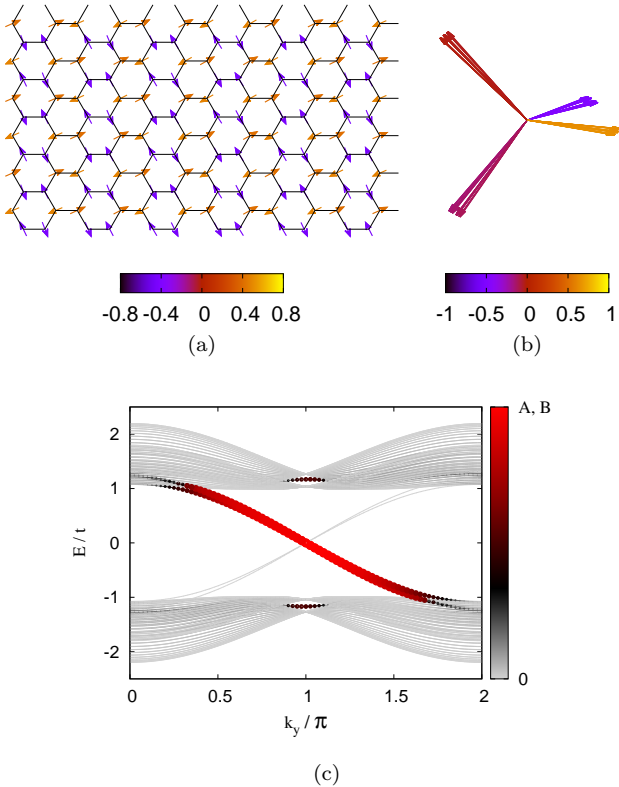


FIG. 7. AFM coupled QAH states. Within each triangular sublattice, hopping $t_2 = 1$ and AFM Heisenberg exchange $J_2 = 0.15$ stabilize the non-coplanar QAH state. Coupling between sublattices is via both kinetic energy $t_1 = 0.2t_2$ and Heisenberg exchange $J_1 = 0.1$, resulting in an overall AFM coupling. As a result, (almost) the same four spin directions arise on both sublattices, see (b), scalar chiralities are the same and edge states on the two sublattices run in parallel. Width and shading of the line in (c) refer to the weight of the left edge of the cylinder and illustrated that two of the edge states are well localized to this edge. (The other two run along the right edge.)

with MCMC simulations occasionally fall in the wrong local minimum. Direct energy comparison reveals that for infinite Hund's rule coupling, the electron-mediated interaction is effectively FM, as one would expect for a double-exchange mechanism, and grows with $|t_1|$. However, it is rather weak and other exchange processes could easily overcome it and induce overall AFM coupling. A natural example would be large but finite Hund's-rule coupling J_{Hund} , where an effective AFM exchange $\propto t_1^2/J_{\text{Hund}}$ arises in second-order perturbation theory⁴²

As both AFM and FM coupling are thus potentially relevant, let us discuss the overall spin pattern and band character in each case. First, we note that MCMC simulations, e.g. for $t_1 = 0.2t_2$ and $J_1 = \pm 0.1$, indicate that the chiral spin pattern within the sublattices is indeed preserved. Second, AFM and FM Heisenberg coupling between the sublattices selects identical or opposite Chern

numbers, resp.: For each B -sublattice spin, the three A -sublattice spins occupying its NN sites are along three of the four directions of the chiral pattern; their combined magnetic moment points in the direction opposite to the fourth and 'missing' spin. For AFM $J_1 > 0$, the B spin will align itself opposite to this combined moment and consequently along said fourth direction. As a result the same four directions arise in each sublattice, see Fig. 7(a,b), where third-neighbor spins are always parallel. Chiralities and Chern numbers of the two sublattices are then the same. Connection of two bands with $C = 1$ into one band with $C = 2$ is natural, two edge state continue to run in parallel, see Fig. 7(c). A very similar phase arising in a Hubbard-like model has been discussed in Ref. 16.

3. Antiferromagnetic topological crystalline insulator protected by time-reversal plus reflection along y direction

For FM $J_1 < 0$, on the other hand, the B spins will align themselves opposite to directions of the A sublattice, making all third-neighbor spins antiparallel. This gives a total of eight spin directions, see Fig. 8(a,b), as well as opposite chiralities. If there were no hopping between the sublattices, i.e. for $t_1 = 0$, this would imply two bands with opposite Chern numbers and edge states running in opposite directions. Since NN hopping t_1 mixes the sublattices, a naturally resulting scenario is that the edge states hybridize and open a gap at the Fermi level when the two bands with $C = \pm 1$ are mixed into a band with $C = 0$. However, this is not quite what happens, as can be seen in Fig. 8(c,d): while the total Chern number is indeed $C = 0$ and while armchair edge states open a gap (as expected), zig-zag edge states do not hybridize and continue to cross each other as well as the Fermi level.

Such a behavior – robust edge states on one edge, but not on the other – suggests a similarity to topological crystalline insulators:²⁶ As a spatial symmetry takes the role that is played by time-reversal invariance in topological insulators, edge states are only protected on edges that share the relevant symmetry. As we are going to see, the phase is actually protected by a combination of a spatial reflection and time inversion, similar to the case of a newly proposed interacting topological state, the topological magnet.⁴³

Within each triangular sublattice, the effective hoppings in the QAH phase show an internal symmetry, so that the four-site magnetic unit cell can be reduced to a two-site electronic unit cell.⁸ On the honeycomb lattice, the unit cell can thus be reduced from eight to four sites. Labeling the two sublattices of the honeycomb lattice by $+$ and $-$ and the two sites of the electronic unit cell within each triangular sublattice by A and B , the kinetic energy $\propto t_2$ can be written in terms of Pauli matrices $\tau^x/y/z$ acting on the electronic sublattice degree of

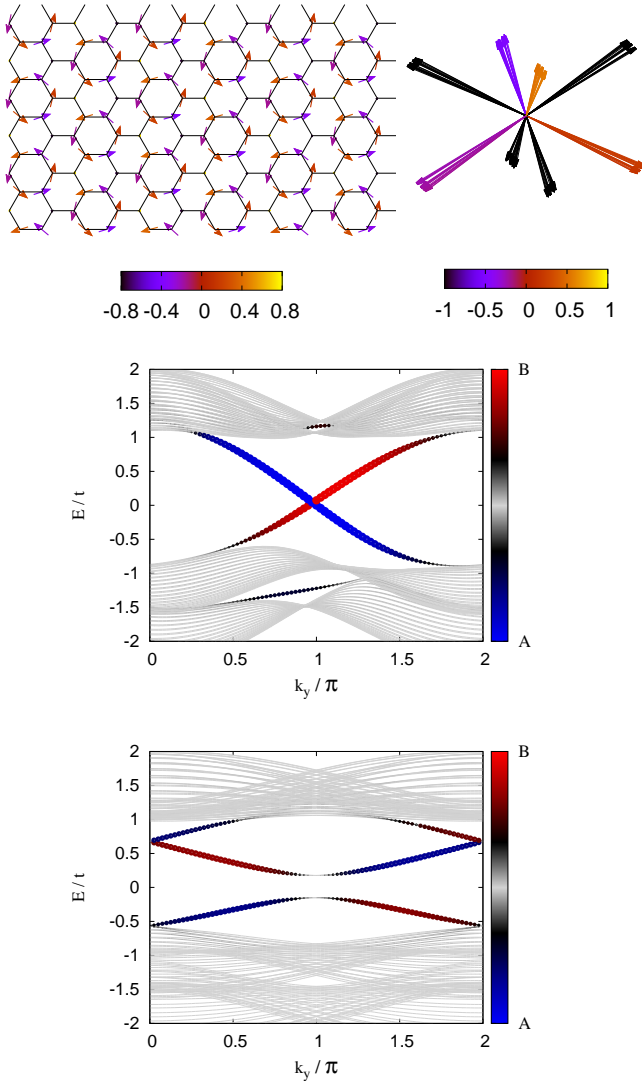


FIG. 8. FM coupled QAH states with $t_1 = 0.2t_2$ and $J_2 = -0.1$, $t_2 = 1$, $J_2 = 0.15$. Spin orientations arising on the two sublattices in (a) are now antiparallel. In (b), where black arrows are for one of the sublattices and lighter ones for the other, this leads to a total of 8 different spin directions. Scalar chiralities are also opposite. Edge states along (c) zig-zag and (d) armchair edges. Line width indicates weight on the edge and shading is chosen according to sublattice character A or B ; the zigzag edge states are each located on one sublattice.

freedom, i.e.,

$$H_2 = \sum_{\vec{k}, \alpha = +, -} \left(c_{\vec{k}, \alpha, A}^\dagger, c_{\vec{k}, \alpha, B}^\dagger \right) \vec{d}_{\vec{k}, \alpha} \cdot \vec{\tau} \begin{pmatrix} c_{\vec{k}, \alpha, A} \\ c_{\vec{k}, \alpha, B} \end{pmatrix}. \quad (3)$$

The vectors $\vec{d}_{\vec{k}, \alpha}$ have entries

$$d_{\vec{k}, \alpha}^z = -\frac{2t_2}{\sqrt{3}} \cos(\vec{k}(\vec{a}_1 - \vec{a}_2)) \quad (4)$$

$$d_{\vec{k}, \alpha}^x = t_2 \sqrt{\frac{2}{3}} (\cos \vec{k} \vec{a}_1 + \cos \vec{k} \vec{a}_2) \quad (5)$$

$$d_{\vec{k}, \pm}^y = \mp t_2 \sqrt{\frac{2}{3}} (\cos \vec{k} \vec{a}_1 - \cos \vec{k} \vec{a}_2), \quad (6)$$

where the sign of $d_{\vec{k}, \alpha}^y$ chooses one of the two chiralities and thus fixes the Chern number of the occupied band. Time reversal acts on this sign. Due to a local gauge freedom, other parameterizations⁴⁴ are possible, but the present one leads to a more symmetric NN hopping, see below. The fact that honeycomb sublattices $+$ and $-$ do not mix, gives Eq. (3) an accidental time-reversal symmetry that is removed by $t_1 \neq 0$.

The kinetic energy of the NN interlattice hopping can be written as

$$H_1 = \sum_{\vec{k}} \left(c_{\vec{k}, +, A}^\dagger, c_{\vec{k}, +, B}^\dagger \right) \begin{pmatrix} h_{AA}^{+-} & h_{AB}^{+-} \\ h_{BA}^{+-} & h_{BB}^{+-} \end{pmatrix} \begin{pmatrix} c_{\vec{k}, -, A} \\ c_{\vec{k}, -, B} \end{pmatrix} + \text{H.c} \quad (7)$$

with matrix elements

$$h_{AA}^{+-}(\vec{k}) = -i(e^{-i\frac{\pi}{12}} e^{i\vec{k}\vec{b}_1} - e^{i\frac{\pi}{12}} e^{i\vec{k}\vec{b}_2}) \quad (8)$$

$$h_{BB}^{+-}(\vec{k}) = -e^{i\frac{\pi}{12}} e^{i\vec{k}\vec{b}_1} + e^{-i\frac{\pi}{12}} e^{i\vec{k}\vec{b}_2} \quad (9)$$

$$h_{AB}^{+-}(\vec{k}) = h_{BA}^{+-}(\vec{k}) = -e^{-i\vec{k}(\vec{b}_1 + \vec{b}_2)}. \quad (10)$$

Time reversal inverts all spins and thus gives the complex conjugate of the position-space hopping elements, but does not take the complex conjugate of the Fourier factors $e^{i\vec{k}\vec{b}_i}$ that are purely due to spatial geometry. The time-reversed matrix elements become thus

$$\mathcal{T}h_{AA}^{+-}(\vec{k}) = i(e^{i\frac{\pi}{12}} e^{i\vec{k}\vec{b}_1} - e^{-i\frac{\pi}{12}} e^{i\vec{k}\vec{b}_2}) \quad (11)$$

$$\mathcal{T}h_{BB}^{+-}(\vec{k}) = -e^{-i\frac{\pi}{12}} e^{i\vec{k}\vec{b}_1} + e^{i\frac{\pi}{12}} e^{i\vec{k}\vec{b}_2} \quad (12)$$

$$\mathcal{T}h_{AB}^{+-}(\vec{k}) = \mathcal{T}h_{BA}^{+-}(\vec{k}) = -e^{-i\vec{k}(\vec{b}_1 + \vec{b}_2)} = h_{AB}^{+-}(\vec{k}). \quad (13)$$

NN hopping Eq. (7) is clearly not time-reversal invariant as $\mathcal{T}h_{XX}^{+-}(\vec{k}) \neq h_{XX}^{+-}(\vec{k})$, but a simultaneous exchange $\vec{b}_1 \leftrightarrow \vec{b}_2$ restores the original matrix elements. As can be seen in Fig. 9, the corresponding operation is a reversal of y direction, i.e., of the direction along a zig-zag edge. This reflection exchanges at the same time vectors $\vec{a}_1 \leftrightarrow \vec{a}_2$ of the triangular sublattices. Equations (3) and (4) indicate that this operation changes the sign of $d_{\vec{k}, \pm}^y$ and thus likewise undoes the effect of time reversal. Both parts of the Hamiltonian are accordingly invariant under a combination of time reversal and reflection of the y -direction and this symmetry protects the edge states along zig-zag edges. Both time and y reversal invert the sign of component k_y along the zig-zag edge, so that the

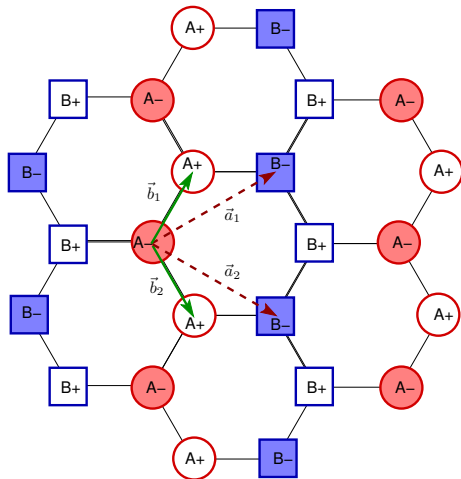


FIG. 9. Sublattice structure underlying the effective electronic Hamiltonian Eqs. (3) - (10). Empty and filled symbols (resp. + and -, as in the main text) indicate the triangular sublattices of the honeycomb lattice, \vec{a}_1 and \vec{a}_2 are basis vectors of the underlying Bravais lattice, $\vec{b}_1 = (2\vec{a}_1 - \vec{a}_2)/3$ and $\vec{b}_2 = (2\vec{a}_2 - \vec{a}_1)/3$ connect NN sites. Circles and squares indicate the magnetic A and B sublattices within each triangular sublattice. Inversion of the y direction switches \vec{b}_1 with \vec{b}_2 and \vec{a}_1 with \vec{a}_2 .

total combined symmetry operation keeps the sign of k_y intact. As a result, the crossing of the edge states is not pinned to high-symmetry momenta like $k_y = 0, \pi$, but can - and does - occur at arbitrary momenta depending on t_1 , see Fig. 8.

Naturally, the question of invariants arises. The total Chern number of these two bands is 0, as discussed above, and in the presence of a sublattice-mixing $t_1 \neq 0$, there is also no sublattice Chern number to take its place. While it is not apparent from Fig. 8, the two occupied bands are almost separated from one another, connected only by a Dirac point. A ‘mass term’, i.e. a staggered onsite potential of opposite sign for the two sublattices, opens a gap at this Dirac point, so that Chern numbers for the two occupied bands can readily be obtained numerically. They are opposite, i.e., one of the occupied (as well as of the empty) bands has $C = 1$ and the other $C = -1$.

Figure 8 shows the edge states for such a case, here with a substantial staggered onsite potential. Making the honeycomb sublattices + and - inequivalent clearly does not affect the topological protection, as also expected from the above symmetry considerations. The zigzag edge states connect pairs of empty and occupied subbands with opposite Chern numbers. Both with and without onsite potential, the edge states are localized on one of the sublattices, even though the bulk bands, which they connect, mix sublattices. This is reminiscent of graphene (without spin-orbit coupling), where the edge-states on zigzag and bearded edges can likewise be assigned to a sublattice and persist for inequivalent sublattices.⁴⁵ In the graphene case, the edge states do not

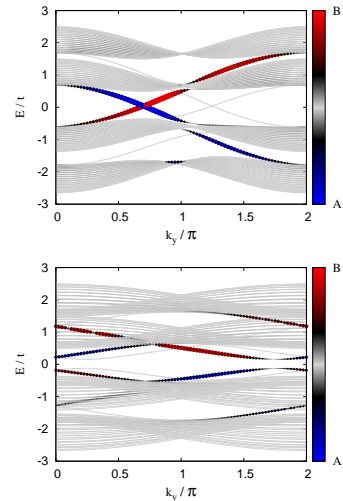


FIG. 10. Edge states for (a) zigzag and (b) armchair edges and the pattern with FM coupling and opposite chirality between the + and - sublattices. Parameters $t_1 = 0.2t_2$, $J_1 = -0.1$, $J_2 = 0.15$, $t_2 = 1$ as in Fig. 8(c,d), but with an additional staggered onsite potential $m = 0.5t_2$ that makes + and - sublattices inequivalent. Monte-Carlo results thus indicate that the phase is stable for moderate $m \neq 0$.

generically cross the Fermi level. Here, where the additional structure (A vs. B) within each sublattice drives the band gap at the Fermi level, they do.

For simplicity, we have here restricted the discussion to the case of infinite Hund’s-rule coupling, where only the spin projection parallel to the local magnetic order is active. If Hund’s-rule coupling is large, but finite, the hoppings between parallel and antiparallel spins require us to use the full eight-site magnetic unit cell in addition to bringing both spin directions into play. The 16×16 matrix makes the discussion more cumbersome, but we have verified that the physics reported here (e.g. protected edge states on zigzag edges) remains valid.

IV. SUMMARY AND CONCLUSIONS

Motivated by materials where frustrated spin and electron systems can be coupled into an unfrustrated, or at least less frustrated, total system, we study the double-exchange model with NN and NNN hopping and spin exchange on the honeycomb lattice. We focus first on the interplay of NN hopping (promoting FM order) with NNN superexchange (frustrated, promoting AFM with a 120° YK pattern): For half filling, the phase diagram is dominated by coplanar, but non-collinear, patterns mostly built up from AFM dimers. For all these states as well as for the limiting FM and YK AFM states, the effective electronic bands remain graphene-like with Dirac cones at the Fermi level.

When discussing a filling of $n = 1/3$ or $n = 2/3$ rather than half filling, density of states at the Fermi level of

the FM state is quite high and we would thus expect the kinetic energy to have a larger impact than at half filling. To some extent, this is indeed what happens: Finite J_2 here induces non-coplanar spin patterns. Such a tendency to non-coplanar order has been observed in frustrated double-exchange models before and is an important difference to purely magnetic frustrated Heisenberg honeycomb models, where states remain coplanar. On the other hand, we find here mostly incommensurate patterns, in contrast to $n = 1/2$ and similar to Heisenberg models.

We then turned our investigation to coupling two triangular-lattice quantum anomalous-Hall states into a honeycomb lattice. For AFM coupling, a Chern insulator with $C = 2$ arises, while FM coupling gives $C = 0$. We find that NN hopping mediates only very small FM coupling. The resulting phase may be related to the $C = 0$ state with non-coplanar magnetism recently reported for the honeycomb Hubbard model¹⁶ and is, however, not topologically trivial despite its vanishing Chern number, see Sec. III B 3. Instead, a combination of time-reversal and mirror-reflection symmetries protects edge states on zig-zag, but not armchair, edges.

The combination of time-reversal and inversion/reflection symmetry protecting a topologically nontrivial state has recently also been discussed as crucial for topologically nontrivial phases in double-perovskites bilayers.⁴⁶ The scenario differs in several instances from our, e.g. concerning the character of the state in question and the origin of nontrivial band topology. Nevertheless, it is intriguing to note that both are systems where frustrated sublattices are connected and where this interplay leads to new topological phases driven by crystal symmetry together with (some variant of) antiferromagnetism.

ACKNOWLEDGMENTS

We gratefully acknowledge stimulating and helpful discussion with J. Venderbos and J. van den Brink. This research was supported by the Deutsche Forschungsgemeinschaft, via the Emmy-Noether program (DA 1235/1-1) and FOR1807 (DA 1235/5-1); by the NSF through Grant Nos. DMR-1506263 and DMR-1506460. SR acknowledges ITF, IFW for computing cluster.

-
- ¹ G. A. Fiete, V. Chua, M. Kargarian, R. Lundgren, A. Rüegg, J. Wen, and V. Zyuzin, *Physica E* **44**, 845 (2012).
² L. Balents, *Nature* **464**, 199 (2010).
³ S. T. Bramwell, *Science* **294**, 1495 (2001).
⁴ Y.-P. Huang, G. Chen, and M. Hermele, *Phys. Rev. Lett.* **112**, 167203 (2014).
⁵ U. K. Rößler, A. N. Bogdanov, and C. Pfleiderer, *Nature* **442**, 797 (2006).
⁶ I. Rousochatzakis, U. K. Rössler, J. van den Brink, and M. Daghofer, *Phys. Rev. B* **93**, 104417 (2016).
⁷ Y. Kamiya and C. D. Batista, *Phys. Rev. X* **4**, 011023 (2014).
⁸ I. Martin and C. D. Batista, *Phys. Rev. Lett.* **101**, 156402 (2008).
⁹ B. G. Ueland, C. F. Miclea, Y. Kato, O. Ayala Valenzuela, R. D. McDonald, R. Okazaki, P. H. Tobash, M. A. Torrez, F. Ronning, R. Movshovich, Z. Fisk, E. D. Bauer, I. Martin, and J. D. Thompson, *Nature Communications* **3**, 1067 (2012).
¹⁰ R. Ozawa, S. Hayami, K. Barros, G.-W. Chern, Y. Motome, and C. D. Batista, *ArXiv e-prints* (2015), arXiv:1510.06830 [cond-mat.str-el].
¹¹ Z. Fang, K. Terakura, and J. Kanamori, *Phys. Rev. B* **63**, 180407 (2001).
¹² R. Morrow, R. Mishra, O. D. Restrepo, M. R. Ball, W. Windl, S. Wurmehl, U. Stockert, B. Büchner, and P. M. Woodward, *J. Am. Chem. Soc.* **135**, 18824 (2013).
¹³ O. N. Meetei, O. Erten, M. Randeria, N. Trivedi, and P. Woodward, *Phys. Rev. Lett.* **110**, 087203 (2013).
¹⁴ B. Yan, A. K. Paul, S. Kanungo, M. Reehuis, A. Hoser, D. M. Többens, W. Schnelle, R. C. Williams, T. Lancaster, F. Xiao, J. S. Möller, S. J. Blundell, W. Hayes, C. Felser, and M. Jansen, *Phys. Rev. Lett.* **112**, 147202 (2014).
¹⁵ S. Nakatsuji, H. Tonomura, K. Onuma, Y. Nambu, O. Sakai, Y. Maeno, R. T. Macaluso, and J. Y. Chan, *Phys. Rev. Lett.* **99**, 157203 (2007).
¹⁶ K. Jiang, Y. Zhang, S. Zhou, and Z. Wang, *Phys. Rev. Lett.* **114**, 216402 (2015).
¹⁷ T. Li, *EPL* **97**, 37001 (2012).
¹⁸ W.-S. Wang, Y.-Y. Xiang, Q.-H. Wang, F. Wang, F. Yang, and D.-H. Lee, *Phys. Rev. B* **85**, 035414 (2012).
¹⁹ A. K. Paul, M. Reehuis, V. Ksenofontov, B. Yan, A. Hoser, D. M. Többens, P. M. Abdala, P. Adler, M. Jansen, and C. Felser, *Phys. Rev. Lett.* **111**, 167205 (2013).
²⁰ I. Martin and C. D. Batista, *Phys. Rev. Lett.* **101**, 156402 (2008).
²¹ S. Kumar and J. van den Brink, *Phys. Rev. Lett.* **105**, 216405 (2010).
²² J. W. Venderbos, M. Daghofer, J. van den Brink, and S. Kumar, *Phys. Rev. Lett.* **107**, 076405 (2011).
²³ E. Rastelli, A. Tassi, and L. Reatto, *Physica B+C* **97**, 1 (1979).
²⁴ J. B. Fouet, P. Sindzingre, and C. Lhuillier, *Eur. Phys. J. B* **20**, 241 (2001).
²⁵ H. Li, H.-F. Song, and Y. Liu, *EPL (Europhysics Letters)* **116**, 37005 (2016).
²⁶ L. Fu, *Phys. Rev. Lett.* **106**, 106802 (2011).
²⁷ For classical spins, antiferromagnetic coupling would lead to an equivalent situation.
²⁸ E. Müller-Hartmann and E. Dagotto, *Phys. Rev. B* **54**, R6819 (1996).

- ²⁹ E. R. Dagotto, T. Hotta, and A. Moreo, *Phys. Rep.* **344**, 1 (2001).
- ³⁰ A. Weiße, *Phys. Rev. Lett.* **102**, 150604 (2009).
- ³¹ When using full diagonalization, we made use of the fact that the low coordination number of the model without NNN hopping permits the use of faster routines for band-diagonal matrices, if sites on the 2D lattice are numbered suitably.
- ³² J. Riera, K. Hallberg, and E. Dagotto, *Phys. Rev. Lett.* **79**, 713 (1997).
- ³³ T. A. Kaplan and S. D. Mahanti, *Journal of Physics: Condensed Matter* **9**, L291 (1997).
- ³⁴ J. Zang, H. Rder, A. R. Bishop, and S. A. Trugman, *Journal of Physics: Condensed Matter* **9**, L157 (1997).
- ³⁵ Z. Nussinov and J. van den Brink, *Rev. Mod. Phys.* **87**, 1 (2015).
- ³⁶ S. Liang, M. Daghofer, S. Dong, C. Şen, and E. R. Dagotto, *Physical Review B* **84**, 024408 (2011).
- ³⁷ R. Ozawa, S. Hayami, and Y. Motome, *Phys. Rev. Lett.* **118**, 147205 (2017).
- ³⁸ D. Xiao, M.-C. Chang, and Q. Niu, *Rev. Mod. Phys.* **82**, 1959 (2010).
- ³⁹ R. Nandkishore, G.-W. Chern, and A. V. Chubukov, *Phys. Rev. Lett.* **108**, 227204 (2012).
- ⁴⁰ E. J. BERGHOLTZ and Z. LIU, *International Journal of Modern Physics B* **27**, 1330017 (2013), <http://www.worldscientific.com/doi/pdf/10.1142/S021797921330017X>.
- ⁴¹ Y. Kato, I. Martin, and C. D. Batista, *Phys. Rev. Lett.* **105**, 266405 (2010).
- ⁴² W. Koller, A. Prüll, H. G. Evertz, and W. von der Linden, *Phys. Rev. B* **66**, 144425 (2002).
- ⁴³ H. Watanabe and L. Fu, *Phys. Rev. B* **95**, 081107 (2017).
- ⁴⁴ S. Kourtis, J. W. Venderbos, and M. Daghofer, *Physical Review B* **86**, 235118 (2012).
- ⁴⁵ W. Yao, S. Yang, and Q. Niu, *Phys. Rev. Lett.* **102**, 096801 (2009).
- ⁴⁶ X.-Y. Dong, S. Kanungo, B. Yan, and C.-X. Liu, *Phys. Rev. B* **94**, 245135 (2016).